ACS APPLIED MATERIALS & INTERFACES

Research Article

www.acsami.org

Synergistic Plasmonic Effects of Metal Nanoparticle–Decorated PEGylated Graphene Oxides in Polymer Solar Cells

Ming-Kai Chuang and Fang-Chung Chen*

Department of Photonics, National Chiao Tung University, Hsinchu 30010, Taiwan

Supporting Information

ABSTRACT: Metal nanostructures that trigger plasmonic near-field effects are often incorporated in organic photovoltaic devices (OPVs) to improve their light-harvesting ability. These nanostructures usually can be positioned in two different locations in a device: (i) within the photon absorption layers and (ii) at the interfaces between the active layer and the metal electrodes. In this study, we developed amphiphilic gold nanoparticles (Au NPs) for use in dual plasmonic nanostructures within OPVs. We employed graphene oxide as the template to anchor the Au NPs, thereby avoiding their aggregation. Furthermore, we added poly(ethylene glycol) (PEG) bis(amine) to the synthesis medium to improve the solubility of the nanocomposites, such that they could be dispersed well in water and in several organic solvents. Accordingly, we could incorporate the PEGylated Au NP/graphene oxides readily into both the buffer layer and photoactive layer of OPVs, which, as a result, exhibited obvious enhancements in their photocurrents and overall device efficiencies. Moreover, we observed different spectral enhancement regions when we positioned the nanocomposites at different locations, reflecting the different dielectric environments surrounding the NPs; this unexpected behavior should assist in enhancing the broadband absorption of solar irradiation.

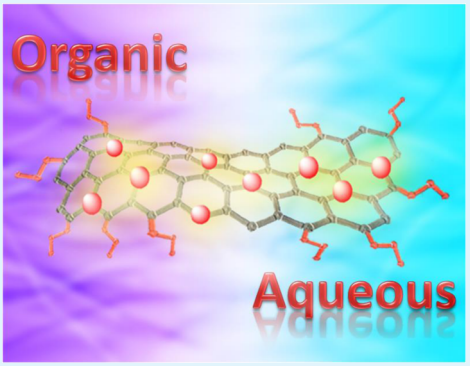

KEYWORDS: *nanoparticle, graphene oxides, plasmonic, solar cells*

1. INTRODUCTION

Bulk heterojunction (BHJ) organic photovoltaic devices (OPVs) receive a great deal of attention because of their potential use as low-cost renewable energy sources that are light in weight and have high mechanical flexibility.[1−5] In the past decade, much effort has been exerted toward developing highly efficient OPVs through various means, including the synthesis of low band gap (LBG) materials for harvesting photons of long wavelength, the design of novel device structures, and control over thin film morphologies.[6−8] Power conversion efficiencies (PCEs) of greater than 10% have been confirmed for single-junction devices;[9] in addition, a triple-junction cell has been reported to function with a PCE exceeding 11%.[10] In the quest to further improve their efficiencies and make OPVs competitive with other thin film solar technologies, many light-trapping techniques—for example, using optical spacers[11,12] and photonic crystals[13]—have also been tested recently. These light-harvesting approaches have become important because organic materials having charge transport lengths that are shorter than the optical absorption length usually lead to insufficient absorption of light. Therefore, the typical thickness of the photoactive layer is usually limited at approximately 100 nm. Further increases in the thickness can result in high series resistances and greater levels of charge recombination because of the low charge mobility of the organic semiconductors.[14,15]

Among strategies for improving light trapping, the use of metallic nanostructures that can support surface plasmons (SPs) is a promising means of increasing the light absorption efficiency of OPVs.[16−18] SPs can be excited either as localized SPs in metal nanoparticles (NPs) or as propagating surface plasmon polaritons at metal−dielectric interfaces.[19] Because the synthesis of NPs is relatively simple, plasmonic-enhanced OPVs are frequently prepared through the direct incorporation of NPs into devices.[17] Because plasmonic nanostructures are readily prepared using solution processes, their fabrication schemes are compatible with those of OPVs—especially for polymer-based devices.

Metal NPs are often positioned at two different locations within OPVs. First, they can be blended directly with the active layer, thereby ensuring the strongest possible near-field effects on the photon absorption layers.[20−22] The morphology of the active layer is, however, often affected when using this approach; serious phase separation may degrade the device performance.[18,23] Second, the NPs can be incorporated into the electrode buffer layers[24−28] or at the interfaces between the photoactive layer and the metal electrodes.[16,29] The drawback of introducing NPs in the vicinity of the active layers is a limited near-field effect because the plasmonic field decays exponentially with the distance from the metal surface.

Received: February 6, 2015
Accepted: March 18, 2015
Published: March 18, 2015

DOI: 10.1021/acsami.5b01161
ACS Appl. Mater. Interfaces 2015, 7, 7397−7405

Scheme 1. Synthesis of Au@PEG−GO Nanocomposites

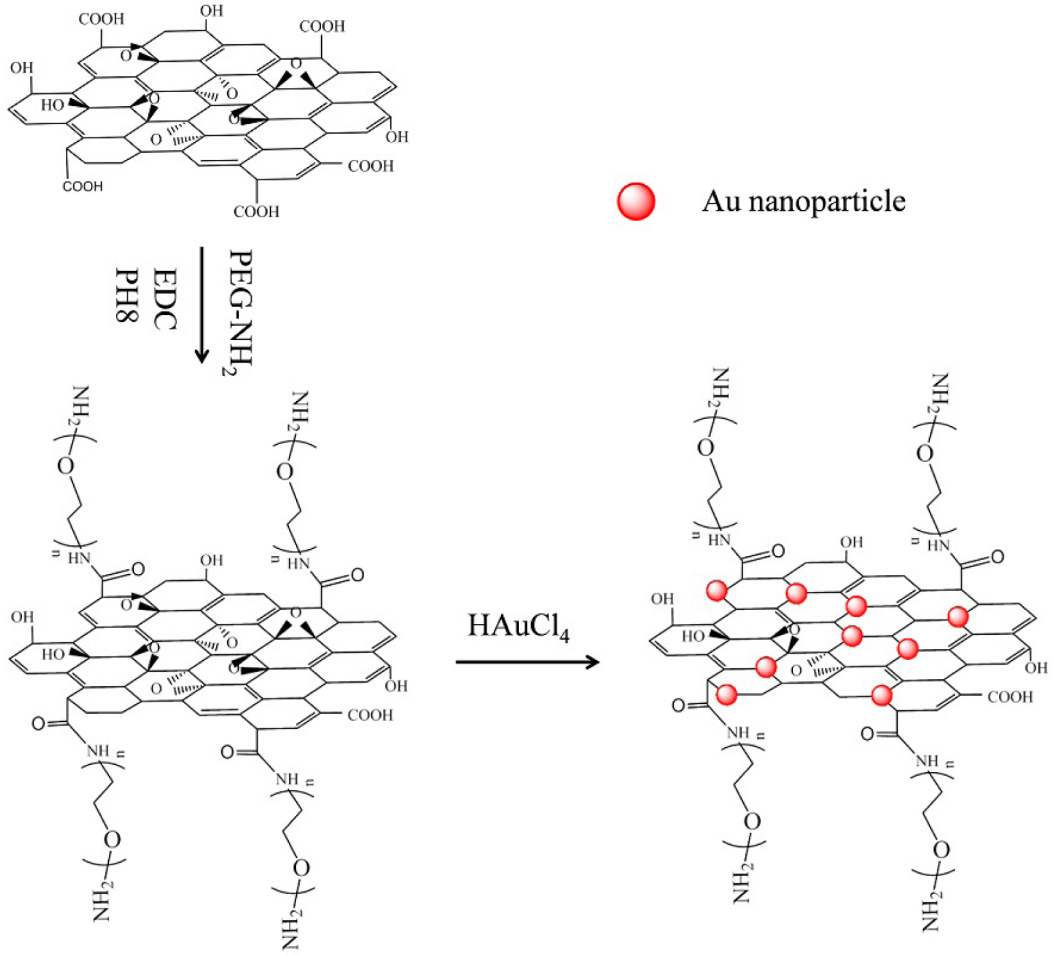

Dual plasmonic nanostructures in a single device have been demonstrated recently.[30−32] Li et al. introduced Au NPs in the active layer and also fabricated Ag nanogratings as the cathode, resulting in accumulated improvements in device performance.[32] Their encouraging results suggested that the development of multiple plasmonic nanostructures might be an effective path toward enhancing the efficiencies of OPVs. The most straightforward approach for realizing dual plasmonic structures would be to blend metal NPs in both the photoactive and buffer layers simultaneously. The fabrication of the two layers, however, usually requires orthogonal solvents to avoid the problem of intermixing. Therefore, the NPs should ideally exhibit amphiphilic solubilities to allow incorporation of sufficient amounts of the plasmonic materials. Furthermore, because metal NPs usually aggregate when they are blended directly into a photoactive layer, high miscibility in the organic matrix is also required to prepare dual nanostructures in a single OPV device.[18]

Graphene and its derivatives, including graphene oxides (GOs), are promising nanoscale building blocks for various functional composite materials.[33] The dispersion of metal NPs on such 2D nanosheets opens up new pathways for developing nanomaterials possessing enhanced catalytic, biomedical, and optoelectronic properties.[34] In particular, the abundance of oxygen-containing functional groups in GOs makes it relatively easy to tailor their functionalities through chemical modification. Recently, amphiphilic graphene derivatives have been synthesized with improved solubilities and dispersion properties.[35−39] For example, modified reduced GOs can be dispersed well in poly(lactic acid) matrices, thereby improving the mechanical properties of the nanocomposites.[38] Liu et al. used PEGylated nanographene oxides for the delivery of water-insoluble cancer drugs; both sides of the hydrophobic nanosheets were accessible for drug binding through simple adsorption, with the poly(ethylene glycol) (PEG) moieties rendering high aqueous solubility and physiological stability.[39]

In this study, we employed GO as a template for the anchoring of Au NPs, thereby avoiding their aggregation.[40] To further improve the solubility, we introduced poly(ethylene glycol) bis(amine) (PEG-NH_2) to disperse the resulting nanocomposites well in water and in several organic solvents. Because of their better processing properties in different types of solvents, we could readily incorporate the PEGylated Au NP/GO composites (Au@PEG−GO) into both the buffer and photoactive layers of OPVs. As a result, we could obtain dual plasmonic nanostructures through simple solution processes, achieving obvious enhancements in photocurrents and overall device efficiencies. More interestingly, when the nanocomposites were positioned at different locations, we observed different spectral regions of efficiency enhancement, presumably because of the different dielectric environments surrounding the NPs. This unexpected property might be useful for enhancing the broadband absorption of light.

DOI: 10.1021/acsami.5b01161
ACS Appl. Mater. Interfaces 2015, 7, 7397−7405

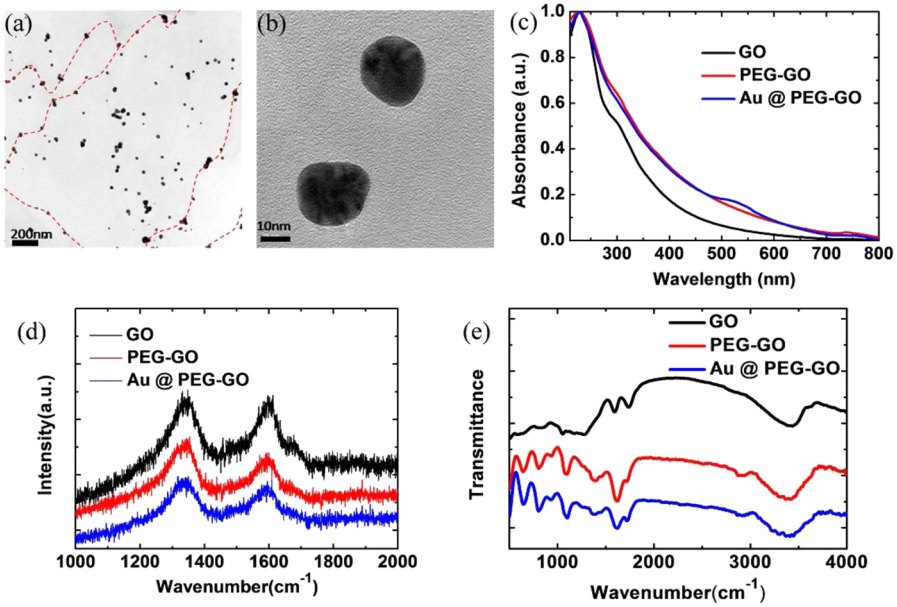

Figure 1. (a) TEM image of Au@PEG−GO nanocomposites. (b) High-resolution TEM image of the Au@PEG−GO nanocomposites. (c) UV−Vis absorption, (d) Raman, and (e) FTIR spectra of GO, PEG−GO, and the Au@PEG−GO nanocomposites.

2. EXPERIMENTAL SECTION

2.1. Synthesis of PEG−GO. The PEGylation synthesis was performed following procedures reported in the literature.[41] First, a solution of PEG-NH_2 (M_w: ca. 6000; 10 mg mL^{-1}, 2 mL) was added into an aqueous solution of GO (0.275 mg mL^{-1}, 10 mL). Next, 1-ethyl-3-(3-(dimethylamino)propyl)carbodiimide (EDC) was added to the mixture to a concentration of 2 mM. The mixture was stirred overnight. The final product was removed through centrifugation and washed twice with deionized (DI) water to remove any unreacted PEG-NH_2. Finally, the product was dried through lyophilization.

2.2. Synthesis of Au@PEG−GO Composites. An aqueous solution of $HAuCl_4$ (0.047 mg mL^{-1}, 10 mL) was mixed with a solution containing the as-prepared PEG−GO (0.9 mg mL^{-1}, 3 mL). The mixture was aged for 30 min to promote interactions between the Au ions and the GO surfaces.[29] The reducing agent, sodium citrate, was added after the mixture had been heated to 80 °C. The solution was stirred for 4 h. The suspension was centrifuged (6000 rpm), and the residue was washed twice with DI water to remove any free Au ions. Finally, the nanocomposites were dried through lyophilization.

2.3. Characterization. Absorption spectra were measured using a UV−Vis−NIR spectrometer (PerkinElmer Lambda 950). XPS spectra were recorded using a PHI 5000 VersaProbe system. FTIR spectra were collected using a Bomem DA8.3 spectrometer. Raman spectra were obtained using a Horoba high-resolution confocal Raman microscope equipped with a HeNe laser. Surface morphologies were observed using a Digital Instruments Dimension 3100 atomic force microscope.

2.4. Device Fabrication and Testing. OPV devices were fabricated on patterned indium tin oxide (ITO)-coated glass substrates. The PEDOT:PSS layer was spin-coated on the ITO-coated glass, and then the sample was baked at 120 °C for 1 h. The photoactive layer, prepared from either a blend of P3HT and $PC_{60}BM$ (1:1, w/w) or a blend of PBDTTT-CT and $PC_{70}BM$ (1:1.5, w/w), was further overcoated on the PEDOT:PSS layer from a solution of DCB. For the preparation of devices containing the GO derivatives, the nanocomposites were blended into the PEDOT:PSS solution and/or the photoactive solution at various concentrations. The wet films of the photoactive polymer blends were subjected to solvent annealing in a glass Petri dish for at least 20 min.[42] The samples were then thermally annealed at 110 °C for 15 min. Finally, the devices were completed through thermal evaporation of Ca (30 nm) and Al (100 nm) as the cathode. The $J-V$ characteristics of the devices were measured using a Keithley 2400 source-measure unit. The photocurrent responses were obtained under illumination from a 150 W Thermal Oriel solar simulator (AM 1.5G). The intensity of the light source was corrected using a standard Si photodiode equipped with a KG5 filter. IPCE spectra were recorded using a measurement system (Enli Technology) comprising a quartz−tungsten−halogen lamp, a monochromator, an optical chopper, and a lock-in amplifier.

3. RESULTS AND DISSCUSSION

Scheme 1 displays our synthetic route toward the amphiphilic Au@PEG−GO nanocomposites. First, the carboxylic acid groups of the GOs were conjugated with PEG-NH_2 through carbodiimide-catalyzed amide formation to improve the dispersibility in organic solvents.[41] The resulting aqueous dispersion of PEGylated graphene oxides (PEG−GOs) was mixed with a $HAuCl_4$ solution and heated at 80 °C. A reducing agent, sodium citrate, was added to the mixture while stirring and heating continuously. After 4 h, the Au salts were reduced, and the resulting Au NPs were attached to the PEG−GO surfaces. Figure S1a and b (Supporting Information) display the results of solubility tests of the Au@PEG−GO nanocomposite and Au NP-decorated GOs (Au@GO) in water and 1,2-dichlorobenzene (DCB), respectively; in each case, the concentration was maintained at 1.0 mg mL^{-1}. Both nanomaterials could be dispersed well in water and DCB after sonication. After standing for 24 h, the Au@GO composite remained well dispersed in water, whereas apparent precipitation was observable in the DCB solution (Figure S1a, Supporting Information). On the other hand, the Au@PEG−GO composite was very stable in both solvents, suggesting that the PEG ligands did improve the solubility in the organic solvents, in part through steric effects preventing restacking of the nanosheets. More results of the solubility tests in various organic solvents can be found in Figure S2 (Supporting Information).

Figure 1a displays transmission electron microscopy (TEM) images of our Au@PEG−GO samples. We observed Au NPs that were distributed uniformly on the GO surfaces, although some aggregated Au nanoclusters were still present. As

DOI: 10.1021/acsami.5b01161
ACS Appl. Mater. Interfaces 2015, 7, 7397−7405

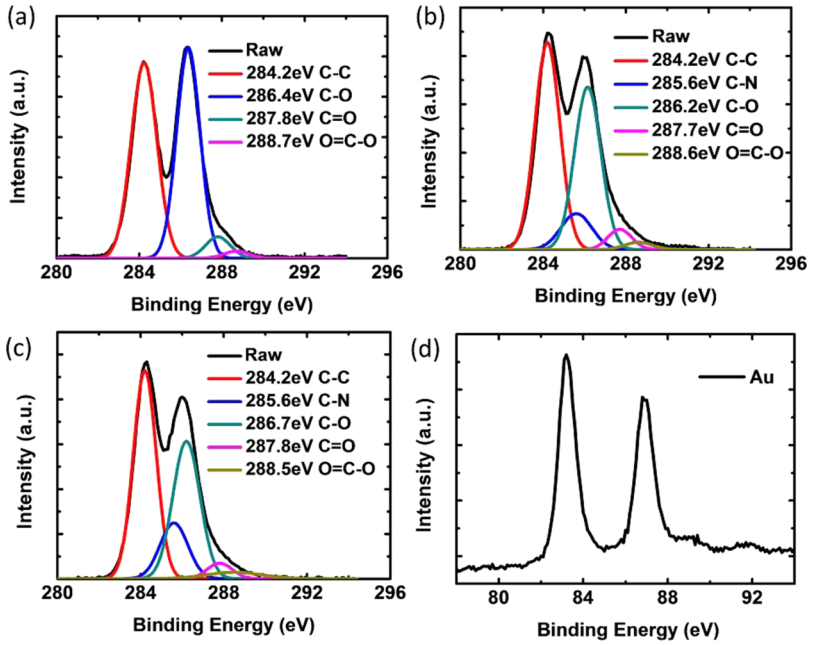

Figure 2. (a–c) C 1s XPS spectra of (a) GO, (b) PEG–GO, and (c) Au@PEG–GO composites. (d) Au 4f XPS spectrum of the Au@PEG–GO sample.

indicated by the dashed lines, which reveal the surfaces of the GOs, the Au NPs were adsorbed on the GOs selectively. We also found that the density of the Au NPs was slightly higher at the edges and at the wrinkles, presumably because their higher numbers of defect sites (e.g., carboxyl groups) provided greater amounts of net negative charge for immobilizing the Au ions during the initial nucleation stage.[43] Furthermore, a high-resolution TEM image (Figure 1b) revealed that the average size of the Au NPs was approximately 22 nm.

We further characterized the Au nanocomposites using various spectroscopic techniques, including UV–Vis absorption spectroscopy, Fourier transform infrared (FTIR) spectroscopy, Raman spectroscopy, and X-ray photoelectron spectroscopy (XPS). The UV–Vis absorption spectra of the Au@PEG–GO solutions (Figure 1c) featured an absorption peak at 525 nm, corresponding to the plasmon band of the Au NPs and confirming the formation of NPs in the suspensions. In addition, all of the solutions exhibited typical absorption peaks at 230 and 305 nm, corresponding to the $\pi-\pi^*$ transitions of C═C bonds and the $n-\pi^*$ transitions of C═O groups, respectively.[44] The absorption spectra of PEG–GO and Au@PEG–GO retained these two characteristic peaks, with no significant spectral shifts, suggesting that no significant structural changes occurred in the GO nanosheets after the PEGylation and reduction steps.

Figure 1d displays Raman spectra of the nanocomposites. Each spectrum featured two typical peaks: a D band (ca. 1330 cm^{-1}) and a G band (ca. 1591 cm^{-1}). The former is associated with the breathing mode of sp^2-hybridized C atoms in rings; the latter is related to the in-plane bond stretching of sp^2-hybridized C atoms.[45,46] Because the D band is also associated with structural disorder and defects, the ratio of the intensities of the D and G bands (I_D/I_G) can be used to probe the extent of in-plane disorder. Table S1 (Supporting Information) lists the I_D/I_G ratios for our various samples. The value for the original GO sample (I_D/I_G = 1.01) increased slightly to 1.05 for the PEG–GO nanocomposite. We suspect that amide formation at the edges of the GO sheets may have slightly altered the electronic conjugation within the graphene sheets. Furthermore, the I_D/I_G ratio of the Au@PEG–GO composite remained almost unchanged after the reduction process, suggesting that the GOs did not undergo reduction under our applied conditions.

Figure 1e presents FTIR spectra of our various GO samples. The spectrum of the GO sample exhibited characteristic peaks near 3400 and 1740 cm^{-1}, corresponding to vibrations of OH and C═O groups, respectively.[47] We assign another peak, near 1590 cm^{-1}, to the stretching vibrations of C═C bonds.[48,49] After PEGlyation, strong signals near 2880 and 1085 cm^{-1} appeared for the PEG–GO composite, representing the symmetric and asymmetric stretching modes of the CH_2 groups and the C–O stretching vibrations, respectively, of the PEG moieties.[41,49] The presence of these two peaks suggests that PEG moieties had indeed been conjugated to the GO sheets. Furthermore, the intensity of the peak for the PEG–GO composite at 1724 cm^{-1}, which we assign to O–C═O vibrations, had decreased significantly; meanwhile, the intensity of the band at 1634 cm^{-1}, which we assign to NH–CO vibrations, increased, consistent with COOH groups having formed amide bonds with PEG–NH_2.[49] Finally, we observed a similar absorption pattern for the Au@PEG–GO after the reduction step, suggesting that decoration with Au NPs did not affect the PEG–GO structure. We also used XPS to further analyze the chemical bonding within these nanomaterials. Figure 2a–c displays the C 1s XPS spectra of the GO nanocomposites. The peak of the neat GO sheets could be deconvoluted into four peaks. The first, centered at 284.2 eV, represented the C–C and C═C bonds; the others, at 286.4, 287.8, and 288.7 eV, can be assigned to the C–O bonds of epoxy and/or alkoxy groups, C═O bonds, and O═C–OH groups, respectively.[49−51] After the PEGylation reaction, another peak appeared, centered at 285.6 eV, that we attribute to the presence of C–N bonds. We also noted that the intensity of the signal for the C–O bonds decreased, suggesting

DOI: 10.1021/acsami.5b01161
ACS Appl. Mater. Interfaces 2015, 7, 7397–7405

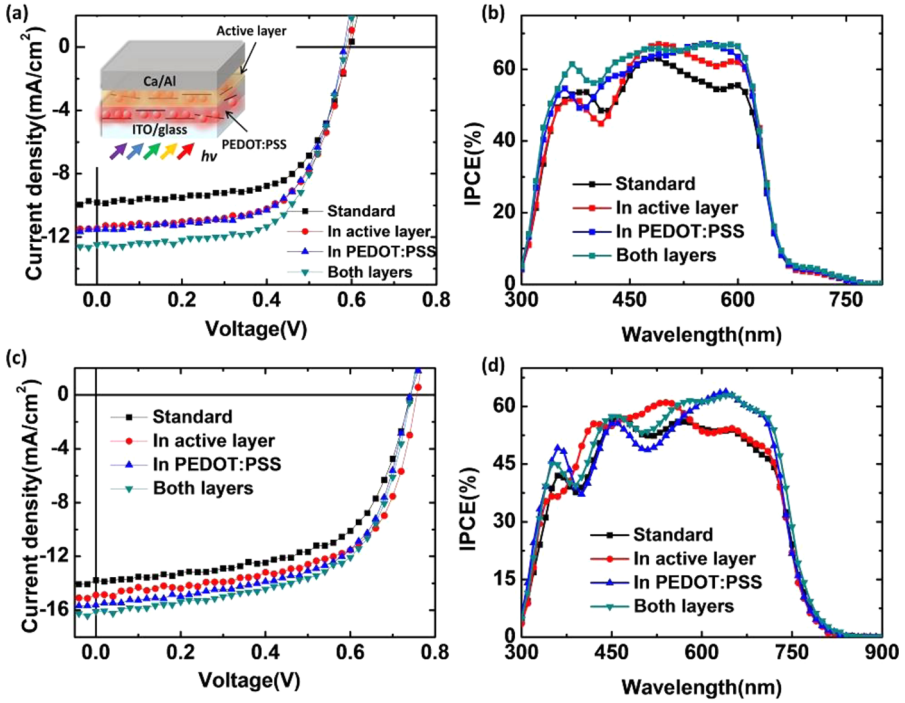

Figure 3. (a) $J-V$ curves of devices under illumination at 100 mW cm^{-1} (AM 1.5G); photoactive layer: P3HT and PCBM. The inset displays the schematic representation of the device structure. (b) Corresponding IPCE curves of the OPV devices in (a). (c) $J-V$ curves of devices based on the PBDTTT-C:PCBM blend and Au@PEG−GO nanocomposites, recorded under AM1.5G illumination. (d) Corresponding IPCE curves of the OPV devices in (c).

Table 1. Electrical Characteristics of Devices Fabricated with Au@PEG−GO Nanocomposites Incorporated into Photoactive Materials or PEDOT:PSS

device	V_{oc} [V]	J_{sc} [mA cm^{-2}]	PCE [%]	FF
standard[a]	0.59 ± 0.01	9.8 ± 0.08	3.70 ± 0.05	0.64 ± 0.01
Au@PEG−GO in active layer[a]	0.59 ± 0.01	11.5 ± 0.21	4.26 ± 0.11	0.63 ± 0.02
Au@PEG−GO in PEDOT layer[a]	0.59 ± 0.01	11.5 ± 0.15	4.40 ± 0.08	0.64 ± 0.01
Au@PEG−GO in active layer and PEDOT layer[a]	0.59 ± 0.01	12.5 ± 0.19	4.66 ± 0.10	0.63 ± 0.01
standard[b]	0.75 ± 0.01	13.8 ± 0.11	6.15 ± 0.06	0.60 ± 0.01
Au@PEG−GO in active layer[b]	0.75 ± 0.01	14.9 ± 0.20	6.92 ± 0.10	0.62 ± 0.01
Au@PEG−GO in PEDOT[b]	0.75 ± 0.01	15.3 ± 0.13	6.94 ± 0.07	0.61 ± 0.01
Au@PEG−GO in active layer and PEDOT layer[b]	0.75 ± 0.01	16.1 ± 0.14	7.26 ± 0.08	0.60 ± 0.01

[a]Photoactive materials: P3HT and $PC_{61}BM$. [b]Photoactive materials: PBDTTT-CT and $PC_{71}BM$.

the removal of oxygen-containing functional groups. These results confirmed the successful PEGylation of the GOs. Moreover, the Au(4f) spectrum of the Au@PEG−GO sample (Figure 2d) featured peaks corresponding to Au $4f_{7/2}$ and Au $4f_{5/2}$ orbitals at 83.2 and 86.9 eV, respectively, supporting the presence of Au^0.[52]

To investigate the plasmonic effects of the nanocomposites on the performance of OPVs, we fabricated devices incorporating our various GO derivatives. The spatial location of metal NPs can be a critical factor affecting the efficiency of a device.[27,32] Because the Au@PEG−GO composite could be dispersed well in both water and DCB, we could readily incorporate them into either the poly(3,4-ethylenedioxythiophene):polystyrenesulfonate (PEDOT:PSS) layer or the active layer. The inset to Figure 3a displays the device structure and illustrates the different spatial locations of the Au@PEG−GO composites. Figure 3a presents the current density−voltage ($J-V$) characteristics of OPVs fabricated with the GO derivatives, under illumination with simulated solar light (100 mW cm^{-1}, AM 1.5G). When the active layer was a P3HT:PCBM blend, the standard device (i.e., the one prepared without any GO derivatives) exhibited an open-circuit voltage (V_{oc}) of 0.59 V, a short-circuit current density (J_{sc}) of 9.82 mA cm^{-2}, and a fill factor (FF) of 0.64, yielding a PCE of 3.70%. After the Au@PEG−GO composite had been blended into the active layer, the value of V_{oc} remained at 0.59 V, suggesting that doping of the NPs did not affect the interface between the active layer and the electrodes. On the other hand, the photocurrent improved to 11.5 mA cm^{-2}, resulting in the PCE increasing to 4.26%. Table 1 summarizes the performance characteristics of the various devices prepared in this study.

To clarify the effect of the metal NPs, we also fabricated devices containing various amounts of PEG−GO but without any Au NPs incorporated within them. Figure S3 (Supporting Information) reveals that, interestingly, the values of V_{oc} and J_{sc} remained almost unchanged upon the addition of the PEG−GO nanosheets. The FF, however, decreased monotonically upon increasing the concentration of PEG−GO. We suspect that the insulating nature of PEG−GO might have somehow affected the device resistances, thereby degrading the device

DOI: 10.1021/acsami.5b01161
ACS Appl. Mater. Interfaces 2015, 7, 7397−7405

performance. The enhancement in efficiency of the device containing the Au@PEG−GO nanocomposites suggests that the Au NPs induced plasmonic effects and improved the light-harvesting ability of the OPVs. The advantageous plasmonic effects overwhelmed the degraded electrical properties.[25]

To further study the underlying mechanism responsible for the enhanced device performance, we measured the incident photon-to-electron conversion efficiency (IPCE) spectra of the various devices (Figure 3b). Compared with the spectrum of the standard device, the IPCEs increased significantly in the range from 500 to 600 nm after incorporation of the Au@PEG−GO materials. The similarity between the spectral ranges for the IPCE and the extinction of the Au NPs (Figure 1c) confirmed that plasmonic effects were occurring in the device featuring Au@PEG−GO. We also used atomic force microscopy (AFM) to examine the morphologies of the active layers before and after the incorporation of the Au@PEG−GO composites. The AFM images in Figure S4 (Supporting Information) do not reveal any significant changes in morphology. Therefore, we conclude that morphological effects were not the main factors behind the enhancement in device performance.

Because of the amphiphilic properties of the Au@PEG−GO nanocomposites, we could also incorporate the NPs into the PEDOT:PSS layer. Figure 3a also displays the $J-V$ characteristics of the OPV after we had doped the Au@PEG−GO composite into the PEDOT:PSS layer. While the values of V_{oc} and FF remained unchanged, the value of J_{sc} increased to 11.5 mA cm^{-2}, resulting in the PCE increasing to 4.40%. More interestingly, if we blended the nanocomposites in both the PEDOT:PSS and P3HT:PCBM layers simultaneously, the photocurrent increased further, to 12.5 mA cm^{-2}, thereby improving the calculated PCE to 4.66%. Overall, the photocurrent increased by greater than 20%.

To explore the potential plasmonic effects of the amphiphilic nanocomposites, we also applied other LBG polymers, such as poly{[4,8-bis(2-ethyl-hexyl-thiophene-5-yl)-benzo[1,2-b:4,5-b′]dithiophene-2,6-diyl]-*alt*-[2-(2′-ethyl-hexanoyl)-thieno[3,4-*b*]thiophen-4,6-diyl]} (PBDTTT-CT), to the fabrication of OPV devices.[53] Figure 3c displays the electrical properties of devices incorporating the PBDTTT-CT/$PC_{71}BM$ blend as the active layer. The standard device exhibited a value of V_{oc} of 0.75 V, a value of J_{sc} of 13.8 mA cm^{-2}, and a FF of 0.60, yielding a PCE of 6.15%. After blending the Au@PEG−GO nanocomposites into the PBDTTT-CT/$PC_{71}BM$ layer, the value of J_{sc} improved to 14.9 mA cm^{-2}; the FF increased slightly to 0.62, resulting in the PCE increasing to 6.92%. Similarly, the PCE improved to 6.94% after we had added the Au@PEG−GO composite into the PEDOT:PSS buffer. When we incorporated the NPs into both layers, we obtained a higher photocurrent (16.1 mA cm^{-2}); the calculated PCE was 7.24%. The IPCE spectra of the PBDTTT-CT:$PC_{71}BM$ devices revealed a trend similar to that of the photocurrent (Figure 3d).

Figure 4 displays the changes in the IPCEs of the OPVs investigated in this study. The ranges of efficiency enhancement changed after we incorporated the Au NPs at different positions in the device. For the P3HT:PCBM-based devices with Au@PEG−GO doped in the PEDOT:PSS layer, the enhancement in efficiency ranged mainly at wavelengths from 520 to 640 nm (Figure 4a). When we incorporated the Au@PEG−GO composite into the active layer, however, we observed a broader spectral region of enhancement. We suspect that this difference was due to the different dielectric environments

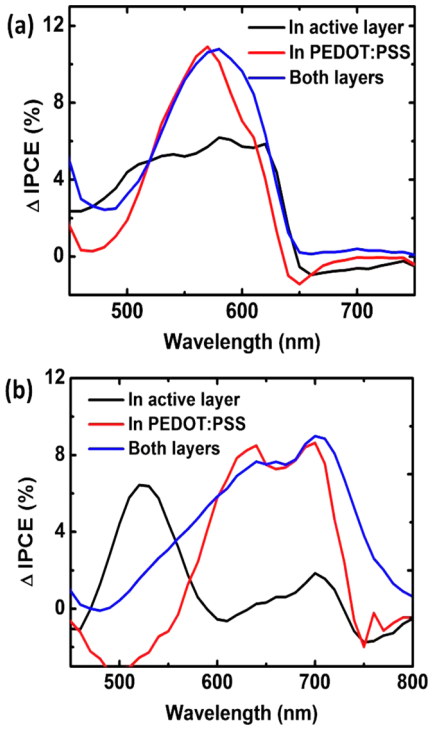

Figure 4. ICPE spectra displaying the changes in IPCE (ΔIPCE) for various plasmonic devices. Active layer: (a) P3HT:PCBM; (b) PBDTTT-C:PCBM.

surrounding the Au NPs.[26,54] Interestingly, the enhancement in quantum efficiencies became higher and broader after we had doped the Au NPs in both layers. In order to study the absorption behavior of the active layers prepared under different conditions, we performed reflectance measurements using various devices; the results are displayed in Figure S5a (Supporting Information).[27] We can observe that the devices containing Au@PEG−GO composites exhibited lower reflectivity than that of the reference device, suggesting more photons were trapped in the devices due to the plasmonic effects. Figure S5b (Supporting Information) also displayed the difference in absorption of these thin films. Similar trends to the IPCE spectra have been observed. Therefore, these results are in good agreement with our proposed plasmonic mechanism.

For the devices prepared using the LBG polymer as the active layer, the differences in the spectral enhancement regions were even more pronounced. As revealed in Figure 4b, doping of the nanocomposite in the active layer (PBDTTT-CT/$PC_{71}BM$) increased the efficiencies relatively strongly near 520 nm. The curve red-shifted and covered the spectral range from 560 to 750 nm. When we doped the NPs in both device locations, the range of enhancement became much more extended. Because solar radiation covers a broad wavelength range, our results suggest that the various dielectric environments surrounding plasmonic nanostructures can be used to extend the spectral range of enhanced light absorption.

Finally, to confirm the plasmonic effects, we also examined the steady state photoluminescence (PL) of photoactive layers prepared under the various experimental conditions (Figure 5a). The PL intensities of the P3HT:PCBM films increased by greater than 20% when we blended the Au@PEG−GO composite into either the PEDOT:PSS layer or the photoactive layer, indicating the presence of apparent plasmonic effects.[23] We suspect that the higher PL intensities were due to the

DOI: 10.1021/acsami.5b01161
ACS Appl. Mater. Interfaces 2015, 7, 7397−7405

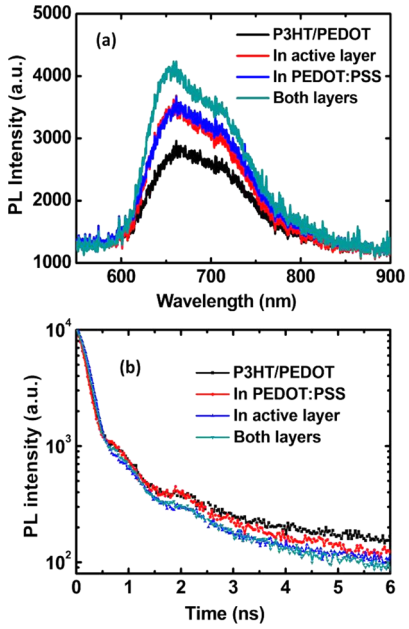

Figure 5. (a) PL spectra of P3HT films incorporating Au@PEG−GO nanocomposites, recorded using an excitation source wavelength of 470 nm. (b) PL decay profiles for P3HT/PCBM films incorporating Au@PEG−GO nanocomposites. Excitation source: 470 nm pulsed laser.

enhanced near fields surrounding the Au NPs, thereby improving the absorption efficiencies of the polymers and, accordingly, increasing the number of excitons.

We also performed time-resolved PL measurements to study the dynamics of the plasmonic effects. Figure 5b displays the PL intensity decay profiles, obtained using a 407 nm pulse laser as the light source, of the photoactive layers prepared under various conditions. We fitted the curves using a multi-exponential function[55]

$$I(t) = \sum_{i=1}^{n} \alpha_i \exp\left(-\frac{t}{\tau_i}\right) \quad (1)$$

where α_i is the amplitude of the ith decay; τ_i is the ith exponential constant; and n is the number of decays involved. All of the decay curves could be fitted well using two exponential constants (τ_1 and τ_2); Table 2 lists the fitting results. For the P3HT:PCBM sample prepared without any blended NPs, the values of τ_1 and τ_2 were 0.191 and 1.765 ns, respectively, corresponding to a exciton lifetime ($\tau_{exciton}$) of 0.819 ns.[55] For the devices prepared with a single nanostructure, namely, with Au@PEG−GO in either the PEDOT:PSS layer or the active layer, the values of $\tau_{exciton}$ decreased to 0.746 and 0.724 ns, respectively. Notably, the value of $\tau_{exciton}$ of the sample containing the Au NPs in the active layer was shorter than that in the PEDOT:PSS layer, presumably because of the near-field nature of the plasmonic effects when the metal surfaces were closer to the excitons. After we had doped the nanocomposites into both layers, the exciton lifetime decreased further to 0.687 ns, suggesting even stronger coupling between the excitons and the plasmonic field.[23] These results confirmed the presence of plasmon−exciton coupling in the devices and, furthermore, the accumulation of the plasmonic effects of the Au NPs at the two different device locations.

Table 2. Exciton Lifetime Constants Determined from the PL Decay Curves in Figure 5b

sample	τ_1 (ns)	τ_2 (ns)	$\tau_{exciton}$ (ns)
reference (no GOs)	0.191	1.765	0.819
Au@PEG−GO in PEDOT:PSS layer	0.186	1.493	0.746
Au@PEG−GO in active layer	0.184	1.413	0.724
Au@PEG−GO in both layers	0.177	1.417	0.687

4. CONCLUSIONS

We have developed Au NP/GO nanocomposites that can be dispersed well in both aqueous and organic solvents. This amphiphilicity is especially suitable for positioning the plasmonic nanomaterials in different layers of conventional OPVs. When we blended these nanocomposites into the PEDOT:PSS layer and/or the active layer, they introduced LSPR effects in the OPVs, leading to excellent enhancements in the photocurrents and efficiencies of the devices under solar irradiation. Because the two layers provided different dielectric environments, the spectral ranges over which the efficiencies were enhanced were different, suggesting a practical method for extending the range of useful wavelengths when applying a single plasmonic material. We hope that this study will open up new avenues for improving the performance and applications of solar cells through the exploitation of LSPR effects.

■ ASSOCIATED CONTENT

Ⓢ Supporting Information

Results of the solubility tests in various aqueous and organic solvents, $J-V$ curves of the devices containing various ratios of PEG−GO nanocomposites, AFM images of the P3HT:PCBM films containing various nanocomposites, and table of the Raman results. This material is available free of charge via the Internet at http://pubs.acs.org.

■ AUTHOR INFORMATION

Corresponding Author

*E-mail: fcchen@mail.nctu.edu.tw. Phone: +886 3 5131484. Fax: +886 3 5735601.

Author Contributions

The manuscript was written through contributions of all authors. All authors have given approval to the final version of the manuscript.

Funding

This study was supported by the Ministry of Science and Technology of Taiwan (Grant Nos.: MOST 102-2221-E-009-130-MY3, MOST 101-2628-E-009-008-MY3, MOST 103-2218-E-009-034) and by the Ministry of Education of Taiwan via the ATU program.

Notes

The authors declare no competing financial interest.

■ REFERENCES

(1) Dennler, G.; Scharber, M. C.; Brabec, C. J. Polymer-Fullerene Bulk-heterojunction Solar Cells. *Adv. Mater.* **2009**, *13*, 1323−1328.

(2) Dou, L.; You, J.; Hong, Z.; Xu, Z.; Li, G.; Street, R. A.; Yang, Y. A Decade of Organic/Polymeric Photovoltaic Research. *Adv. Mater.* **2013**, *25*, 6642−6671.

(3) Yip, H. L.; Jen, A. K.-Y. Recent Advances in Solution-processed Interfacial Materials for Efficient and Stable Polymer Solar Cells. *Energy Environ. Sci.* **2012**, *5*, 5994−6011.

DOI: 10.1021/acsami.5b01161
ACS Appl. Mater. Interfaces 2015, 7, 7397−7405

(4) Krebs, F. C.; Espinosa, N.; Hösel, M.; Søndergaard, R. R.; Jørgensen, M. Rise to Power − OPV-Based Solar Parks. *Adv. Mater.* **2014**, *26*, 29−39.
(5) Graham, K. R.; Cabanetos, C.; Jahnke, J. P.; Idso, M. N.; Labban, A. E.; Ndjawa, G. O. N.; Heumueller, T.; Vandewal, K.; Salleo, A.; Chmelka, B. F.; Amassian, A.; Beaujuge, P. M.; McGehee, M. D. Importance of the Donor:Fullerene Intermolecular Arrangement for High-Efficiency Organic Photovoltaics. *J. Am. Chem. Soc.* **2014**, *136*, 9608−9618.
(6) Hawks, S. A.; Deledalle, F.; Yao, J.; Rebois, D. G.; Li, G.; Nelson, J.; Yang, Y.; Kirchartz, T.; Durrant, J. R. Relating Recombination, Density of States, and Device Performance in an Efficient Polymer:-Fullerene Organic Solar Cell Blend. *Adv. Energy Mater.* **2013**, *3*, 1201−1209.
(7) Dang, M. T.; Hirsch, L.; Wantz, G.; Wuest, J. D. Controlling the Morphology and Performance of Bulk Heterojunctions in Solar Cells. Lessons Learned from the Benchmark Poly(3-hexylthiophene):[6,6]-Phenyl-C_{61}-butyric Acid Methyl Ester System. *Chem. Rev.* **2013**, *113*, 3734−3765.
(8) Guo, Z.; Lee, D.; Schaller, R. D.; Zuo, X.; Lee, B.; Luo, T.; Gao, H.; Huang, L. Relationship between Interchain Interaction, Exciton Delocalization, and Charge Separation in Low-Bandgap Copolymer Blends. *J. Am. Chem. Soc.* **2014**, *136*, 10024−10032.
(9) Li, G.; Zhu, R.; Yang, Y. Polymer Solar Cells. *Nat. Photonics* **2012**, *6*, 153−161.
(10) Chen, C. C.; Chang, W. H.; Yoshimura, K.; Ohya, K.; You, J.; Gao, J.; Hong, Z.; Yang, Y. An Efficient Triple-Junction Polymer Solar Cell Having a Power Conversion Efficiency Exceeding 11%. *Adv. Mater.* **2014**, *26*, 5670−5677.
(11) Kim, J. Y.; Kim, S. H.; Lee, H. H.; Lee, K.; Ma, W.; Gong, X.; Heeger, A. J. New Architecture for High-efficiency Polymer Photovoltaic Cells using Solution-based Titanium Oxide as an Optical Spacer. *Adv. Mater.* **2006**, *18*, 572−576.
(12) Chen, F. C.; Wu, J. L.; Hung, Y. Spatial Redistribution of the Optical Field Intensity in Inverted Polymer Solar Cells. *Appl. Phys. Lett.* **2010**, *96*, 193304.
(13) Ko, D. H.; Tumbleston, J. R.; Gadisa, A.; Aryal, M.; Liu, Y.; Lopez, R.; Samulski, E. T. Light-Trapping Nano-Structures in Organic Photovoltaic Cells. *J. Mater. Chem.* **2011**, *21*, 16293−16303.
(14) Blom, P. W. M.; Mihailetchi, V. D.; Koster, L. J. A.; Markov, D. E. Device Physics of Polymer:Fullerene Bulk Heterojunction Solar Cells. *Adv. Mater.* **2007**, *19*, 1551−1556.
(15) Li, W.; Hendriks, K. H.; Roelofs, W. S.; Kim, Y.; Wienk, M. M.; Janssen, R. A. Efficient Small Bandgap Polymer Solar Cells with High Fill Factors for 300 nm Thick Films. *Adv. Mater.* **2013**, *25*, 3182−3186.
(16) Gan, Q.; Bartoli, F. J.; Kafafi, Z. H. Plasmonic-Enhanced Organic Photovoltaics: Breaking the 10% Efficiency Barrier. *Adv. Mater.* **2013**, *25*, 2385−2396.
(17) Stratakis, E.; Kymakis, E. Nanoparticle-Based Plasmonic Organic Photovoltaic Devices. *Mater. Today* **2013**, *16*, 133−146.
(18) Chou, C. H.; Chen, F. C. Plasmonic Nanostructures for Light Trapping in Organic Photovoltaic Devices. *Nanoscale* **2014**, *6*, 8444−8458.
(19) Atwater, H. A.; Polman, A. Plasmonics for Improved Photovoltaic Devices. *Nat. Mater.* **2010**, *9*, 205−213.
(20) Wang, D. H.; Kim, D. Y.; Choi, K. W.; Seo, J. H.; Im, S. H.; Park, J. H.; Park, O. O.; Heeger, A. J. Enhancement of Donor−Acceptor Polymer Bulk Heterojunction Solar Cell Power Conversion Efficiencies by Addition of Au Nanoparticles. *Angew. Chem., Int. Ed.* **2011**, *50*, 5519−5523.
(21) Li, X.; Choy, W. C. H.; Lu, H.; Sha, W. E. I.; Ho, A. H. P. Efficiency Enhancement of Organic Solar Cells by Using Shape-Dependent Broadband Plasmonic Absorption in Metallic Nanoparticles. *Adv. Funct. Mater.* **2013**, *21*, 2728−2735.
(22) Chen, H. C.; Chou, S. W.; Tseng, W. H.; Chen, I. W. P.; Liu, C. C.; Liu, C.; Liu, C. L.; Chen, C. H.; Wu, C. I.; Chou, P. T. Large AuAg Alloy Nanoparticles Synthesized in Organic Media Using a One-Pot Reaction: Their Applications for High-Peformance Bulk Heterojunction Solar Cells. *Adv. Funct. Mater.* **2012**, *22*, 3975−3984.
(23) Xue, M.; Li, L.; Tremolet de Villers, B. J.; Shen, H.; Zhu, J.; Yu, Z.; Stieg, A. Z.; Pei, Q.; Schwartz, B. J.; Wang, K. L. Charge-Carrier Dynamics in Hybrid Plasmonic Organic Solar Cells with Ag Nanoparticles. *Appl. Phys. Lett.* **2011**, *98*, 253302.
(24) Chen, F. C.; Wu, J. L.; Lee, C. L.; Hung, Y.; Kuo, C. H.; Huang, M. H. Plasmonic-Enhanced Polymer Photovoltaic Devices Incorporating Solution-Processable Metal Nanoparticles. *Appl. Phys. Lett.* **2009**, *95*, 013305.
(25) Wu, J. L.; Chen, F. C.; Hsiao, Y. S.; Chien, F. C.; Chen, P.; Kuo, C. H.; Huang, M. H.; Hsu, C. S. Surface Plasmonic Effects of Metallic Nanoparticles on the Performance of Polymer Bulk Heterojunction Solar Cells. *ACS Nano* **2011**, *5*, 959−967.
(26) Kao, C. S.; Chen, F. C.; Liao, C. W.; Huang, M. H.; Hsu, C. S. Plasmonic-Enhanced Performance for Polymer Solar Cells Prepared with Inverted Structures. *Appl. Phys. Lett.* **2012**, *101*, 193902.
(27) Choi, H.; Lee, J. P.; Ko, S. J.; Jung, J. W.; Park, H.; Yoo, S.; Park, O.; Jeong, J. R.; Park, S.; Kim, J. Y. Multipositional Silica-Coated Silver Nanoparticles for High-Performance Polymer Solar Cells. *Nano Lett.* **2013**, *13*, 2204−2208.
(28) Fung, D. D. S.; Qiao, L.; Choy, W. C. H.; Wang, C.; Sha, W. E. I.; Xie, F.; He, S. J. Optical and Electrical Properties of Efficiency Enhanced Polymer Solar Cells with Au Nanoparticles in a PEDOT−PSS Layer. *J. Mater. Chem.* **2011**, *21*, 16349−16356.
(29) Chuang, M. K.; Lin, S. W.; Chen, F. C.; Chu, C. W.; Hsu, C. S. Gold Nanoparticle-Decorated Graphene Oxides for Plasmonic-Enhanced Polymer Photovoltaic Devices. *Nanoscale* **2014**, *6*, 1573−1579.
(30) Xie, F. X.; Choy, W. C. H.; Wang, C. C. D.; Sha, W. E. I.; Fung, D. D. S. Improving the Efficiency of Polymer Solar Cells by Incorporating Gold Nanoparticles into all Polymer Layers. *Appl. Phys. Lett.* **2011**, *99*, 153304.
(31) Liu, C. M.; Chen, C. M.; Su, Y. W.; Wang, S. M.; Wei, K. H. The Dual Localized Surface Plasmonic Effects of Gold Nanodots and Gold Nanoparticles Enhance the Performance of Bulk Heterojunction Polymer Solar Cells. *Org. Electron.* **2013**, *14*, 2476−2483.
(32) Li, X.; Choy, W. C. H.; Huo, L.; Xie, F.; Sha, W. E. I.; Ding, B.; Guo, X.; Li, Y.; Hou, J.; You, J.; Yang, Y. Plasmonic Nanostructures for High Performance Inverted Organic Solar Cells. *Adv. Mater.* **2012**, *24*, 3046−3052.
(33) Zhu, Y.; Murali, S.; Cai, W.; Li, X.; Suk, J. W.; Potts, J. R.; Ruoff, R. S. Graphene and Graphene Oxide: Synthesis, Properties, and Applications. *Adv. Mater.* **2010**, *22*, 3906−3924.
(34) Muszynski, R.; Seger, B.; Kamat, P. V. Decorating Graphene Sheets with gold Nanoparticles. *J. Phys. Chem. C* **2008**, *112*, 5263−5266.
(35) Qi, X.; Pu, K. Y.; Li, H.; Zhou, X.; Wu, S.; Fan, Q. L.; Liu, B.; Boey, F.; Huang, W.; Zhang, H. Amphiphilic Graphene Composites. *Angew. Chem., Int. Ed.* **2010**, *49*, 9426−9429.
(36) Shen, J.; Hu, Y.; Li, C.; Qin, C.; Ye, M. Synthesis of Amphiphilic Graphene Nanoplatelets. *Small* **2009**, *5*, 82−85.
(37) He, T. C.; Qi, X. Y.; Chen, R.; Wei, J.; Zhang, H.; Sun, H. D. Enhanced Optical Nonlinearity in Noncovalently Functionalized Amphiphilic Graphene Composites. *ChemPlusChem.* **2012**, *77*, 688−693.
(38) Ahn, B. K.; Sung, J.; Li, Y.; Kim, N.; lkenberry, M.; Hohn, K.; Mohanty, N.; Nguyen, P.; Sreeprasad, T. S.; Kraft, S.; Berry, V.; Sun, X. S. Synthesis and Characterization of Amphiphilic Reduced Graphene Oxide with Epoxidized Methyl Oleate. *Adv. Mater.* **2012**, *24*, 2123−2129.
(39) Liu, D. Z.; Robinson, J. T.; Sun, X.; Dai, H. PEGylated Nanographene Oxide for Delivery of Water-Insoluble Cancer Drugs. *J. Am. Chem. Soc.* **2008**, *130*, 10876−10877.
(40) Fan, G. Q.; Zhuo, Q. Q.; Zhu, J. J.; Xu, Z. Q.; Cheng, P. P.; Li, Y. Q.; Sun, X. H.; Lee, S. T.; Tang, J. X. Plasmonic-Enhanced Polymer Solar Cells Incorporating Solution-Processable Au Nanoparticle-Adhered Graphene Oxide. *J. Mater. Chem.* **2012**, *22*, 15614−15619.

DOI: 10.1021/acsami.5b01161
ACS Appl. Mater. Interfaces 2015, 7, 7397−7405

(41) Zhang, L.; Wang, Z.; Lu, Z.; Shen, H.; Huang, J.; Zhao, Q.; Liu, M.; He, N.; Zhang, Z. PEGylated Reduced Graphene Oxide as a Superior ssRNA Delivery System. *J. Mater. Chem. B* **2013**, *1*, 749−755.
(42) Chen, F. C.; Ko, C. J.; Wu, J. L.; Chen, W. C. Morphological Study of P3HT:PCBM Blend Films Prepared through Solvent Annealing for Solar Cell Applications. *Sol. Energy Mater. Sol. Cells* **2010**, *94*, 2426−2430.
(43) Hong, W.; Bai, H.; Xu, Y.; Yao, Z.; Gu, Z.; Shi, G. Preparation of Gold Nanoparticle/Graphene Composites with Controlled Weight Contents and Their Application in Biosensors. *J. Phys. Chem. C* **2010**, *114*, 1822−1826.
(44) Luo, Z.; Lu, Y.; Somers, L. A.; Johnson, A. T. C. High Yield Preparation of Macroscopic Graphene Oxide Membranes. *J. Am. Chem. Soc.* **2009**, *131*, 898−899.
(45) Esfandiar, A.; Akhavan, O.; Irajizad, A. Melatonin as a Powerful Bio-Antioxidant for Reduction of Graphene Oxide. *J. Mater. Chem.* **2011**, *21*, 10907−10914.
(46) Ferrari, A. C.; Robertson, J. Interpretation of Raman Spectra of Disordered and Amorphous Carbon. *Phys. Rev. B* **2000**, *61*, 14095−14107.
(47) Wang, X.; Huang, P.; Liu, H.; Li, C.; Shen, G.; Cui, D. Metal Ion-Directed Solution-Phase Tailoring: from Large-Area Graphene Oxide into Nanoscale Pieces. *Nanoscale Res. Lett.* **2013**, *8*, 226.
(48) Zhang, Z.; Chen, H.; Xing, C.; Guo, M.; Xu, F.; Wang, X.; Gruber, H. J.; Zhang, B.; Tang, J. Sodium Citrate: A Universal Reducing Agent for Reduction/Decoration of Graphene Oxide with Au Nanoparticles. *Nano Res.* **2011**, *4*, 599−611.
(49) Bose, S.; Kuila, T.; Mishra, A. K.; Kim, N. H.; Lee, J. H. Dual Role of Glycine as a Chemical Functionalizer and a Reducing Agent in the Preparation of Graphene: an Environmentally Friendly Method. *J. Mater. Chem.* **2012**, *22*, 9696−9703.
(50) Sun, X. M.; Liu, Z.; Welsher, K.; Robinson, J. T.; Goodwin, A.; Zaric, S.; Dai, H. J. Nano-Graphene Oxide for Cellular Imaging and Drug Delivery. *Nano. Res.* **2008**, *1*, 203−212.
(51) Chuang, M. K.; Chen, F. C.; Hsu, C. S. Gold Nanoparticle−Graphene Oxide Nanocomposites that Enhance the Device Performance of Polymer solar Cells. *J. Nanomater.* **2014**, *2014*, 736879.
(52) Geng, M.; Zhang, Y.; Huang, Q.; Zhang, B.; Li, Q.; Li, W.; Li, J. Functionalization of C_{60} with Gold Nanoparticles. *Carbon* **2010**, *48*, 3570−3574.
(53) Guo, X.; Zhang, M.; Ma, W.; Ye, L.; Zhang, S.; Liu, S.; Ade, H.; Huang, F.; Hou, J. Enhanced Photovoltaic Performance by Modulating Surface Composite in Bulk Heterojunction Polymer solar Cells Based on PBDTTT-C-T/PC_{71}BM. *Adv. Mater.* **2014**, *26*, 4043−4049.
(54) Kelly, K. L.; Coronado, E.; Zhao, L. L.; Schatz, G. C. The Optical Properties of Metal Nanoparticles: The Influence of Size, Shape, and Dielectric Environment. *J. Phys. Chem. B* **2003**, *107*, 668−677.
(55) Jones, M.; Nedeljkovic, J.; Ellingson, R. J.; Nozik, A. J.; Rumbles, G. Photoenhancement of Luminescence in Colloidal CdSe Quantum Dot Solutions. *J. Phys. Chem. B* **2003**, *107*, 11346−11352.

DOI: 10.1021/acsami.5b01161
ACS Appl. Mater. Interfaces 2015, 7, 7397−7405